7T MRI

ERWIN L. HAHN INSTITUTE FOR MAGNETIC RESONANCE IMAGING

ANNUAL REPORT

2018

Erwin L. Hahn Institute for Magnetic Resonance Imaging
Kokereiallee 7
45141 Essen
Germany

fon +49 (0) 201 1836070
fax +49 (0) 201 1836073
hahn-institute.de

Published by the Erwin L. Hahn Institute for Magnetic Resonance Imaging.

Preface

It has been a productive year at the Erwin L Hahn Institute, with no major arrivals or departures. The major activity was the preparation of the application to upgrade our 7T system. After prolonged discussions with manufacturers it was decided to apply for a completely new system. This delayed submission of the proposal compared to the original timeline. Harald Quick has been the lead Principal Investigator on this proposal, and we are all hopeful that his hard work will bear fruit in the coming year.

This year's Erwin L Hahn lecture was given by Prof. Klaus Scheffler of the Max Planck Institute for Biological Cybernetics in Tübingen, with the title: *"Human Brain MRI at 9.4T: the pros and cons of ultra high fields"*. This gave a fascinating overview of technical developments and applications at 9.4T, and was the undoubted highlight of a day that saw many outstanding lectures. The 2019 lecture will take place on 6th November, so please reserve this day in your agendas, as it promises to be another memorable event!

This year's annual report covers a broad range of subjects representing the diversity of the PI groups working at the Institute, but also the synergies. There are applications to body (shoulder and pelvis) and brain as well as work on the fundamental questions of safety. Considerable effort has been expended on the development of a new transmit/receive coil for the head with the ability to optimally image the brain stem and cerebellum. This should enable better structural and high spatial resolution functional imaging of the brain. The latter will be important for the further development of one of the Institutes main themes: laminar fMRI, which is reported on by two groups. The combined use of the new hardware and methods, all developed in house opens intriguing possibilities for future research.

I hope you enjoy reading this report, and look forward to another year of progress at the Erwin L Hahn Institute!

David Norris

Essen, January 2019

Clinical shoulder MR imaging at 7 Tesla in comparison to arthroscopy and 1.5 Tesla MRI

Musculoskeletal ultra-high field MR imaging has already demonstrated clinical potential and benefits for knee, wrist, and ankle, i.e. joints which can be relatively easy imaged with local RF coils enclosing the whole structure to be imaged. On the other hand, joints like the hip or shoulder are much more difficult to image at 7T since they are more prone to the challenges at UHF, namely B1+ inhomogeneities and limited penetration depths. Furthermore, dedicated RF coils are not commercially available so far. However, scientists at the ELH institute have a long history of targeting these difficult regions and establishing both RF hardware and imaging protocols [1-9]. A recent publication introduced a two-array RF coil setup for shoulder imaging featuring an 8-channel transmit/receive coil based on microstrip lines with meanders, due to their minimal coupling and high transmit efficiency, and a 7-channel receive-only coil based on loop elements to boost signal-to-noise ratio and acceleration capabilities (Fig. 1) [10]. With this RF coil setup we have acquired high-resolution 7T shoulder images with excellent image quality in healthy volunteers (Fig. 2). The logical next step is of course to assess potential clinical benefits from 7T MRI of the shoulder. Hence, in cooperation with a surgeon, eight patients presenting with shoulder pain in the orthopedic outpatient department of the University Hospital Essen were imaged at the ELH institute. Image quality was assessed in consensus by two radiologists separately for each patient and each sequence. Additionally, a structured report focusing on the rotator cuff was generated in consensus by the same radiologists, assessing fatty atrophy of the rotator cuff muscles, supraspinatus atrophy, the subacromial subdeltoideal bursa, lesions of the tendons, degeneration of acromioclavicular (AC) joint, effusion of the glenohumeral joint, as well as the status of the cartilage, and the labrum. The outcome of the report was afterwards compared with the arthroscopical report taken as the gold standard. Finally, pathologies found at 7T were visually compared with preexisting 1.5T MR images from the same patients.

Figure 1: RF coil setup for shoulder imaging using a C-shaped 8-channel TxRx meander stripline coil (A) in combination with a 7-channel Rx-only loop array (B). In (C), positioning of a subject within the shoulder coil is shown.

Our results showed very good image quality with hardly definable artifacts in PD-weighted TSE sequences with fat suppression, while moderate artifacts appeared in MEDIC and STIR sequences. The most homogenous B1+ field was observed in T1-weighted GRE and DESS sequences. Strongest inhomogeneities appeared in MEDIC and PD-weighted TSE. Likewise, with the exception of vessels and nerves, the delineation of anatomic structures was best in PD-weighted TSE with fat suppression. For vessels and nerves PD-weighted TSE and T1-weighted GRE were rated best, while fat saturated PD TSE sequences underperformed. For the evaluation of muscle tissue, DESS and T1-weighted GRE could complement fat-saturated PD-weighted TSE sequences.

Pathologies of the rotator cuff were identified at 7T in every patient. In correlation with the arthroscopical report, pathologies of the rotator cuff tendons were widely overdiagnosed with 7T MRI: With arthroscopy, tendinitis or partial tear of the supraspinatus tendon was confirmed in only 3 of 8 patients, of the infraspinatus tendon in 0 of 1 patient

Oliver Kraff, Andrea Lazik-Palm, Sascha Beck, Stefan H.G. Rietsch, Konrad Körsmeier, Michael Kamminga, Jens M. Theysohn, Harald H. Quick

According to arthroscopy, only one pathology of the rotator cuff (partial lesion of the subscapularis tendon) was missed with 7T MRI. Pathologies of the long bicipital tendon, the AC-joint. the glenohumeral cartilage, the labrum and the subacromial subdeltoideal bursa were mainly concordant in arthroscopy and 7T MRI. Exceptions were one lesion of the long bicipital tendon, one subacromial bursitis and one SLAP-lesion missed at 7T. Preexisting 1.5T MRI images could be collected from three patients. The delay between the two examinations was 34, 34 and 49 days, respectively. The main pathologies were visible at both field strengths. However, at 7T pathologies were more distinct due to better contrast and higher image resolution (Fig. 3). In conclusion, feasibility of clinical 7T MRI of the shoulder was demonstrated. A comprehensive protocol should include fat saturated PD TSE sequences (excellent delineation of almost all anatomical structures) in axial and coronal orientation and a DESS sequence (isotropic high resolution and muscle delineation). A T1 GRE may complement the protocol for its good depiction of vessels and nerves, while the use of STIR needs to be postponed until substantial optimization yields better results. This comprehensive protocol results in a clinically relevant total acquisition time of 25 minutes.

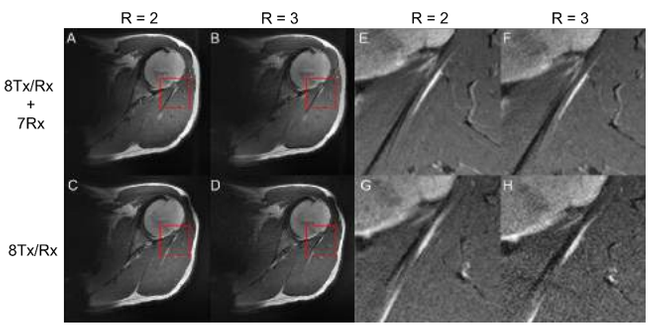

Figure 2: Impact of different acceleration factors on measurements of a healthy volunteer for the 2D TSE sequence using both arrays (top row) and only the 8-channel Tx/Rx coil (bottom row). As expected, increasing the acceleration leads to reduced SNR in each case, but the combination of both arrays can compensate the SNR loss much better due to the lower g-factors. This is especially prominent in the zoomed region (E–H).

References: 1. Kraff O, Lazik-Palm A, Heule R, Theysohn JM, Bieri O, Quick HH (2016) 7 Tesla quantitative hip MRI: a comparison between TESS and CPMG for T2 mapping. Magn Reson Mater Phy 29 (3):503-512. 2. Kraff O, Theysohn JM, Maderwald S, Saylor C, Ladd SC, Ladd ME, Barkhausen J (2007) MRI of the knee at 7.0 Tesla. Rofo 179 (12):1231-1235.3. Lazik A, Theysohn JM, Geis C, Johst S, Ladd ME, Quick HH, Kraff O (2016) 7 Tesla quantitative hip MRI: T1, T2 and T2* mapping of hip cartilage in healthy volunteers. Eur Radiol 26 (5):1245-1253. 4. Lazik-Palm A, Kraff O, Geis C, Johst S, Goebel J, Ladd ME, Quick HH, Theysohn JM (2016) Morphological imaging and T2 and T2* mapping of hip cartilage at 7 Tesla MRI under the influence of intravenous gadolinium. Eur Radiol. 5. Lazik-Palm A, Kraff O, Johst S, Quick HH, Ladd ME, Geis C, Korsmeier K, Landgraeber S, Theysohn JM (2016) Morphological and Quantitative 7 T MRI of Hip Cartilage Transplants in Comparison to 3 T-Initial Experiences. Invest Radiol 51 (9):552-559. 6. Theysohn JM, Kraff O, Maderwald S, Kokulinsky PC, Ladd ME, Barkhausen J, Ladd SC (2013) MRI of the ankle joint in healthy non-athletes and in marathon runners: image quality issues at 7.0 T compared to 1.5 T. Skeletal Radiol 42 (2):261-267. 7. Theysohn JM, Kraff O, Orzada S, Theysohn N, Classen T, Landgraeber S, Ladd ME, Lauenstein TC (2013) Bilateral hip imaging at 7 Tesla using a multi-channel transmit technology: initial results presenting anatomical detail in healthy volunteers and pathological changes in patients with avascular necrosis of the femoral head. Skeletal Radiol 42 (11):1555-1563. 8. Theysohn JM, Kraff O, Theysohn N, Orzada S, Landgraeber S, Ladd ME, Lauenstein TC (2014) Hip imaging of avascular necrosis at 7 Tesla compared with 3 Tesla. Skeletal Radiol 43 (5):623-632. 9. Kraff O, Bitz AK, Dammann P, Ladd SC, Ladd ME, Quick HH (2010) An eight-channel transmit/receive multipurpose coil for musculoskeletal MR imaging at 7 T. Med Phys 37 (12):6368-10. Rietsch SHG, Pfaffenrot V, Bitz AK, Orzada S, Brunheim S, Lazik-Palm A, Theysohn JM, Ladd ME, Quick HH, Kraff O (2017) An 8-channel transceiver 7-channel receive RF coil setup for high SNR ultrahigh-field MRI of the shoulder at 7T. Med Phys 44 (12):6195-6208.

Figure 3: Impingement syndrome of the right shoulder at 7T and 1.5T. In the coronal PD-weighted fat saturated 7T image, narrowing of the subacromial space caused by a small osteophyte (A) can be seen, and signal alterations with areas of high signal intensity in the supraspinatus tendon (B) suggest a partial tendon tear. The following arthroscopy confirmed the bone spur at the ventral basis of the acromion with narrowing of the subacromial space and a partial delamination of the footprint of the supraspinatus tendon. Besides, signs of acromioclavicular joint arthrosis are obvious with irregularities of the cartilage surface, joint fluid and edema of the joint capsule (C).

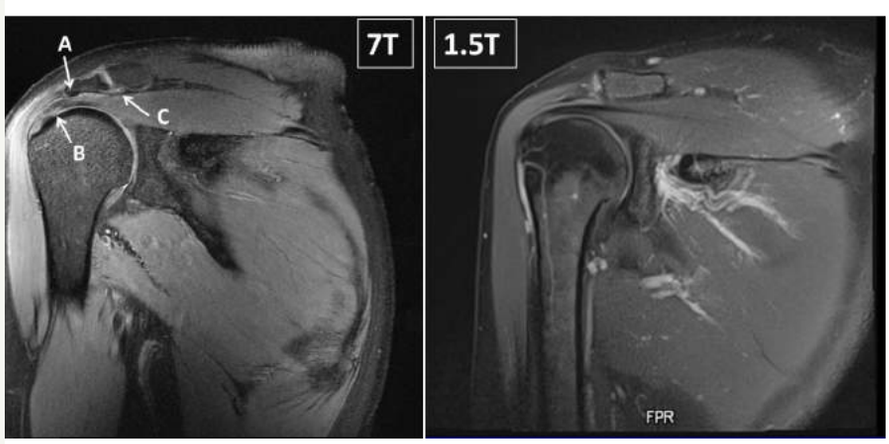

Safety of subjects during RF exposure in UHF MRI

The trend toward higher magnetic field strength (SNR increases more than linearly with B_0) leads to challenges in the safety of subjects with regard to RF exposure at ultra-high-field (UHF) MRI. During exposure to RF fields, energy is absorbed in the electrically lossy body tissue, causing tissue heating. The energy absorbed by the tissue increases with increasing frequency. Furthermore, spatial variations of the RF field distributions are more pronounced with higher frequency.

Limits for the permissible increase in the body core temperature as well as the maximum local tissue temperature are specified in the IEC standard [1]. Alternatively, the heat input into the tissue can be directly limited by using the specific absorption rate (SAR) as a measure. However, whereas the correlation between tissue temperature and possible tissue damage is fairly direct, the correlation between SAR and tissue damage is less explicit.

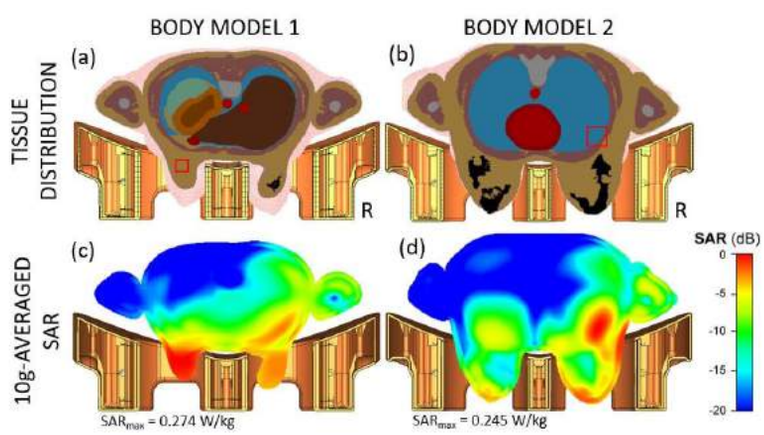

Figure 1: Tissue distribution and 10g-averaged SAR in transversal slice showing the SAR maximum. The volume of the maximum 10g-SAR is marked with a red square in the tissue plot, with the volume being larger in areas with lower tissue density.

In this work, the relationship between local SAR and temperature distribution in the human body during RF exposure was investigated [2]. Overall, the goal was to evaluate whether SAR and temperature distributions correlate inside the human body, whether SAR or temperature is more conservative with respect to the IEC limits, and what the effect of new standards, i.e. in the form of thermal dose, would be on MR imaging at UHF. With the thermal dose, both the temperature and the exposure time are taken into account when assessing possible tissue damage. In the model CEM43°C, the transient temperature profile is scaled to equivalent exposure duration at a reference temperature, and limits for maximum permissible exposure time at the reference temperature are defined.

The correlation between SAR and tissue temperature was investigated using an exposure scenario during 7 Tesla MR mammography with a local transmit/receive breast coil as an example [3]. Since the breast is predominantly composed of low-perfused fat tissue, it may be difficult for the thermal regulation system of the body to compensate for any RF-induced heating. New anatomical body models were generated for the study. 3 Tesla MR images of healthy volunteers with a resolution of 1.2 mm were segmented into 17 different tissue types. The torso and breasts of the body models vary in shape, size and weight, resulting in different loading of the coil. The distribution of material in the breasts also showed large variation, especially regarding the volume ratio between mammary gland and fat tissue. Mammary gland tissue has a higher permittivity and electrical conductivity compared to the surrounding fat tissue.

Local SAR, averaged over 10 g of body tissue, was calculated for the body models. The SAR maximum was located at different body positions: in one model the SAR maximum was in the mamma, while in the other models the SAR maximum was in the torso at the border between lung and muscle tissue (Fig. 1).

Thermal simulations were performed using the simulated SAR distributions as the RF heat source, with the input power corresponding to the SAR limits of the IEC standard [1] (Fig. 2).

Thomas M. Fiedler, Mark E. Ladd, Andreas K. Bitz

The simulations were also used to determine the maximum permissible input power based on local temperature limits from the IEC standard. For the calculation of the local tissue temperature, different temperature-dependent regulation systems proposed in the literature were considered that are intended to model the thermoregulation system of healthy as well as impaired subjects. An impaired thermoregulation system, for example, can be modelled with constant blood perfusion at the basal level. For healthy regulation systems, both a linear perfusion model and an exponential perfusion model were assumed. It was shown that not only the spatial distributions of SAR and local temperature differ, but also the temperature distributions obtained for the different blood perfusion models. The results indicate that the maximum permissible transmission power based on the temperature limits can be higher or lower compared to the SAR limits depending on the perfusion model. Thus, it is necessary to utilize validated models of the thermoregulation system that take into account the subject's health condition.

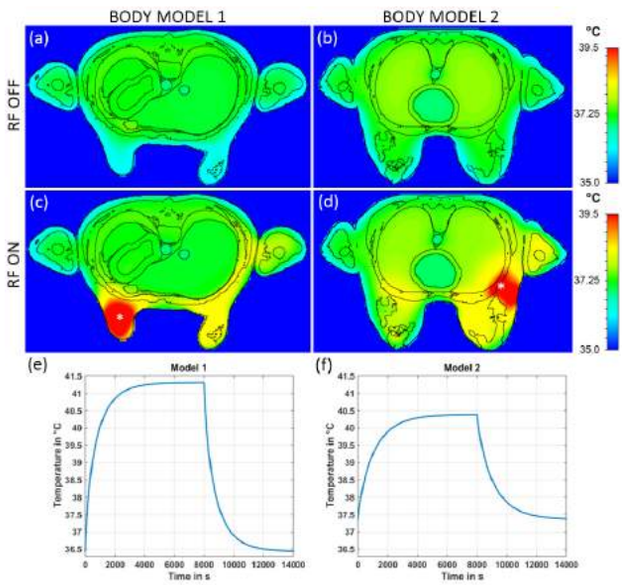

Figure 2: Temperature distribution in steady state without RF exposure (a, b) and with RF exposure (c, d) for two body models and constant blood perfusion. RF power was scaled to the 10 W/kg SAR limit. (e, f) shows the temperature plots versus time for the position of maximum temperature. The temperature maxima are marked with a white asterisk.

Assuming RF input power given by the SAR limit of 10 W/kg, the safety assessment based on the thermal dose allows for exposure times in all configurations that would be longer than any typical examination time, even though the temperature limits are exceeded (see table). For the exponential perfusion model, the permissible exposure times are particularly long. Therefore, for almost all scenarios considered, the constraints on maximum permissible input power are less restrictive when considering thermal dose compared to safety assessments based on either SAR or local tissue temperature. The results are part of the PhD thesis "Safety of subjects during radiofrequency exposure in ultra-high-field magnetic resonance imaging" submitted by Thomas Fiedler to the University of Wuppertal. Thomas Fiedler was awarded the 2018 Best PhD Thesis of the Year Award by the IEEE Germany Section EMC Society Chapter for this thesis.

		Body model 1			Body model 2		
Blood perfusion model:		**constant**	**linear**	**exp.**	**constant**	**linear**	**exp.**
Tissue temperature at $SAR_{10g,max}$ of	0 W/kg	37.6 °C	37.6 °C	37.49 °C	37.61 °C	37.61 °C	37.49 °C
	10 W/kg	41.3 °C	40.5 °C	38.6 °C	40.4 °C	40 °C	38.9 °C
	20 W/kg	46.17 °C	42.18 °C	39.63 °C	44 °C	41.32 °C	39.9 °C
Variation in power to reach temperature limit of	39 °C	-46%	-46%	+37%	-46%	-46%	+2%
	40 °C	-62%	-59%	+40%	-56%	-50%	+10%
Time to reach CEM43°C = 2 min at $SAR_{10g,max}$ of	10 W/kg	58 min			113 min		
	20 W/kg	12 min			21 min		
Time to reach CEM43°C = 9 min at $SAR_{10g,max}$ of	10 W/kg		6 h	> 2 d		10 h	40 h
	20 W/kg		47 min	> 18 h		110 min	11 h

References: 1. IEC 60601-2-33, Edition 3.2. 2015 Medical electrical equipment – Part 2-33: Particular requirements for the basic safety and essential performance of magnetic resonance equipment for medical diagnosis 2. T. M. Fiedler, M. E. Ladd, A. K. Bitz 2018, SAR simulations and safety. Review Article, NeuroImage: Special Issue "Neuroimaging with Ultra-High Field MRI: Present and Future", Volume 168, March 2018, Pages 33-58, DOI: 10.1016/j.neuroimage.2017.03.035 3. T. M. Fiedler, M. E. Ladd, A. K. Bitz 2017, RF safety assessment of a bilateral 4-channel transmit/receive 7 Tesla breast coil: SAR versus tissue temperature limits. Medical Physics, DOI: 10.1002/mp.12034

The research leading to these results has received funding from the European Research Council under the European Union's Seventh Framework Programme (FP/2007-2013) / ERC Grant Agreement n. 291903 MRexcite.

In vivo MR imaging of pelvic lymph nodes at ultra-high magnetic field (7T)

The distribution of MR visible lymph nodes in the pelvis of young volunteers

The presence of metastases of primary cancers in pelvic lymph nodes is a crucial step in disease progression1. Currently, staging of lymph nodes is performed with diagnostic lymph node dissections. A reliable non-invasive imaging method to detect metastases in pelvic lymph nodes would be of great benefit in the field of oncology. In the context of the ongoing debate2 on the validity and therapeutic effect of pelvic lymph node dissections, the current study was performed to define an in vivo nodal anatomical baseline for validation of representative lymph node dissections and accompanying pathology reports, as well as for assessing a potential therapeutic effect of extended lymph node dissections.

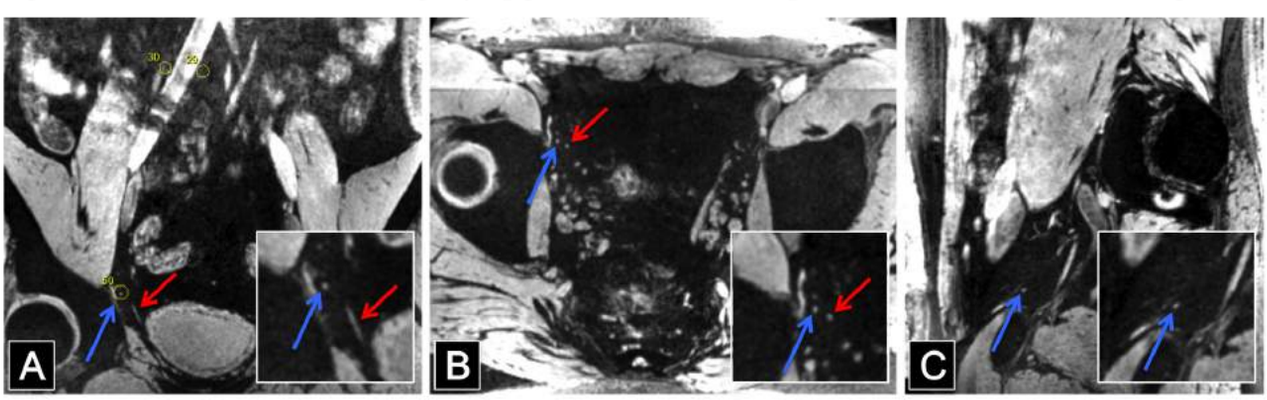

Figure 1: Water-selective images of the pelvis of a healthy volunteer. (A) Coronal image with magnified detail in box. Yellow circle around the detected lymph node. (B) Transversal image with detail box. (C) Sagittal image with detail box. In all images the blue arrow points at a small lymph node, the red arrow at a blood vessel.

We used 2 static alternating RF shims at 7 Tesla for homogeneous pelvic imaging3 in 11 young healthy volunteers (mean age 31, range 25-39 years). After administration of 20 mg Butylscopolamine i.m. the volunteers were measured with a custom-made 8-channel TxRx body-array coil4. An advanced imaging protocol with water-selective iron-sensitive computed echo time (TE) imaging and lipid-selective imaging was developed5 to perform 3D MRI at a spatial resolution of 0.66x0.66x0.66mm3 to detect nodal structures in the pelvis. For water-selective imaging 5 echoes were acquired using a multi-gradient echo (mGRE) sequence from which, after fitting an exponential R2*-decay using a Weighted Linear Least Squares (WLLS) algorithm6, computed echo time images were reconstructed at various TEs.

The water and lipid selective image series were evaluated by 2 readers separately (ASF, ML or/and BP), after which consensus opinion was obtained by both readers together. The water-selective computed TE image set was used to detect and measure lymph nodes. The lipid-selective image set supported the distinction of lymph nodes from surrounding structures, for example blood vessels or ganglia. Number and short axis diameter of detected nodes was measured and size distribution in each of six anatomical regions was assessed, and an average volunteer-normalized nodal size distribution was determined.

In total, 564 lymph nodes were detected in six pelvic regions of the 11 volunteers (representative images in Fig. 1). The mean number was

Ansje Fortuin, Bart Philips, Marloes van der Leest, Mark E. Ladd, Harald H. Quick, Jelle Barentsz, Stefan Rietsch, Sascha Brunheim, Stephan Orzada, Marnix Maas, Tom W.J. Scheenen

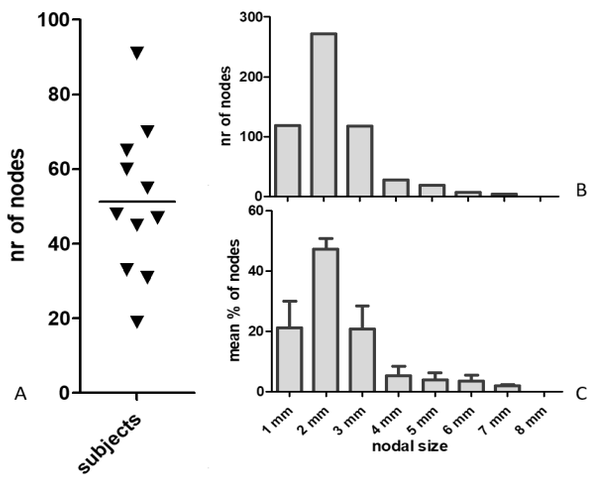

Figure 2. The number and size of pelvic lymph nodes in 11 volunteers. (A) Number of nodes in each subject. (B) Size distribution of 564 lymph nodes. (C) Relative nodal size distribution: the mean (+ SD) of the individual relative size distributions of 11 subjects.

51.3 with a wide range of 19-91 lymph nodes per volunteer. Mean diameter was 2.3 mm with a range of 1 to 7 mm. 69% of the lymph nodes were 2 mm or smaller. The overall size distribution was very similar to the average volunteer-normalized nodal size distribution (Fig. 2). Most and on average largest lymph nodes were detected in the external iliac artery region (mean number 12.4, mean size 3.0 mm) and least as well as smallest lymph nodes were detected in the presacral region (mean number 5.9, mean size 1.7 mm) (Fig. 3).

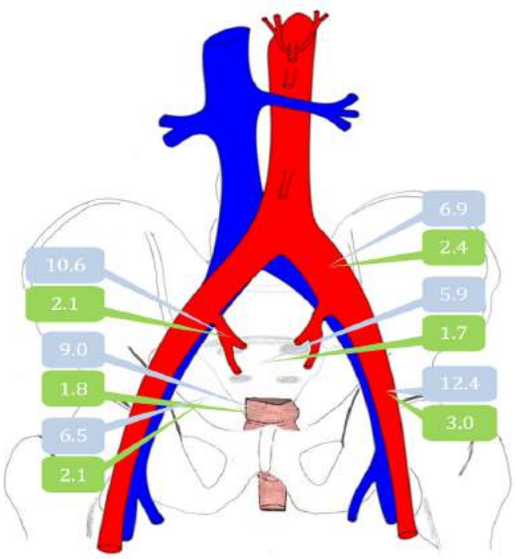

Figure 3. Mean number of lymph nodes per region in light blue, mean lymph node size in green. Indicated regions from top left to bottom right: Internal iliac artery region, Pararectal region, Obturator region, Common iliac artery region, Presacral region, External iliac artery region.

The number of in vivo visible lymph nodes varies largely between subjects, whereas the normalized size distribution of nodes does not. The presence of many small lymph nodes (≤2 mm) in all anatomical regions in the pelvis renders representative or complete removal of pelvic lymph nodes extremely difficult. The value of extended lymph node dissections in the pelvis is under debate, both from a diagnostic perspective as well as from a treatment perspective. With this work, we could question the current validity of representative lymph node dissections and accompanying pathology reports by setting the in vivo nodal anatomical baseline in young volunteers.

References: 1. McMahon CJ, Rofsky NM, Pedrosa I (2010) Lymphatic metastases from pelvic tumors: anatomic classification, characterization, and staging. Radiology 254:31-46 2. Fossati N, Willemse PM, van den Broeck T, et al. The benefits and harms of different extents of lymph node dissection during radical prostatectomy for prostate cancer: a systematic review. Eur Urol. 2017;72(1):84-109. 3. Orzada S, Maderwald S, Poser BA, Bitz AK, Quick HH, Ladd ME. RF excitation using time interleaved acquisition of modes (TIAMO) to address B1 inhomogeneity in high-field MRI. Magn Reson Med 2010;64(2):327-333. 4. Orzada S, Quick HH, Ladd ME, Bahr A, Bolz T, Yazdanbakhsh P, Solbach K, Bitz AK. A flexible 8-channel transmit/receive body coil for 7 T human imaging 2009; Honolulu, Hawaii, USA. p 2999. 5. Philips BWJ, Fortuin AS, Orzada S, Scheenen TWJ, Maas MC. High resolution MR imaging of pelvic lymph nodes at 7 Tesla. Magn Reson Med 2017;78(3):1020-1028. 6. Veraart J, Sijbers J, Sunaert S, Leemans A, Jeurissen B. Weighted linear least squares estimation of diffusion MRI parameters: strengths, limitations, and pitfalls. Neuroimage 2013;81:335-346.

A 32-channel transmit/receive radiofrequency (RF) head coil for 7T UHF MRI

Introduction

7T ultrahigh-field (UHF) MRI provides an increase in signal-to-noise ratio (SNR) (1). The increase of the Larmor frequency at 7T, however, requires multi-channel RF technology and methodology for homogeneous signal excitation. In this context, 32 independent RF transmit channels (2) offer the possibility to acquire homogeneous images at 7T by employing parallel transmit techniques (pTx) (3,4). In this work, a 32-channel transmit/receive (32Tx32Rx) head coil to cover both head and neck was developed and evaluated. First results are presented, demonstrating high degrees of freedom for RF shimming as well as promising anatomical coverage for 7T neuro MRI applications.

Methods

The 32Tx32Rx head coil consists of an 8-channel anterior part (Figure 1A) and a 24-channel posterior part (Figure 1B) and features 32 Tx/Rx loop elements. The anterior part can be opened to facilitate patient positioning. The coil housing is a combination of 3D-printed components that fit he head geometry and flat polycarbonate sheets. Each of the transceiver loop elements of the 32Tx-32Rx coil is connected to a custom-built transmit/receive switch (Figure 1C). This transmit/receive switch consists of a low-noise preamplifier (Wantcom, Chanhassen, MN, USA), which is (in addition to the internal protection) protected by a PIN-diode and a lambda-over-four transmission line. Eight transmit/receive switches are housed in an independent polycarbonate box (Figure 1C). Altogether, 4 of these transmit/receive boxes are used to connect the 32-channel Tx/Rx coil to a custom-built transmit chain add-on (2) and to the receive channels of the MR system. The transmit/receive switches can also be used with any other transmit/receive coil at 7T. All MR measurements were acquired on a 7T whole-body MRI system (Magnetom 7T, Siemens Healthcare GmbH, Erlangen, Germany). The performance of the 32Tx32Rx head coil was compared to a commercial 1Tx32Rx head coil with a single transmit-only birdcage and 32 receive-only loops (Nova Medical, Wilmington, MA, USA). For the 32Tx32Rx coil, B1+ mapping was accomplished using the

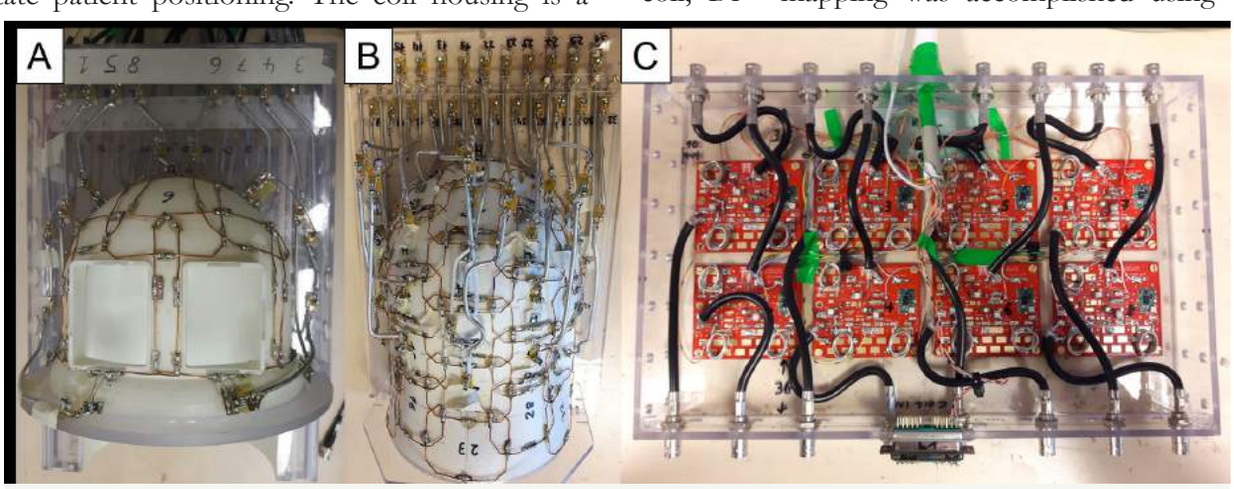

Figure 1: The presented 32-channel transmit/receive coil consists of an anterior part with eight loop elements (A) and a posterior part with 24 loop elements (B). For easy patient positioning the anterior part can be moved along z-direction. The connection between transmit/receive switches and loops is accomplished by semi-rigid coaxial cables and cable traps (A,B). Each RF coil element is connected to a transmit/receive switch (C). Eight of those switches are housed in a polycarbonate box (C), of which four are used for 7T measurements with the 32Tx32Rx head coil.

Stefan H.G. Rietsch, Stephan Orzada, Sascha Brunheim, Andreas K. Bitz, Maximilian N. Völker, Viktor Pfaffenrot, Marcel Gratz, Oliver Kraff, Mark E. Ladd, Peter J. Koopmans, Harald H. Quick

loops (Nova Medical, Wilmington, MA, USA). For the 32Tx32Rx coil, B1+ mapping was accomplished using the B1TIAMO approach by Brunheim et al. (5).

Results and Discussion

The flip angle distributions (Figure 2A,C) demonstrate the obstacles for a comparison between a 1-channel transmit birdcage (Figure 2A) and a 32-channel TxRx coil (Figure 2C). The transmit voltage was adjusted such that comparable flip angle is achieved in the entire transversal slice (white dotted circle in Figure 2C) for both coils (Figure 2A,C). While the RF shim for the 32Tx32Rx head coil was successfully optimized for homogeneity in the entire transversal slice, the CP+ excitation by the commercial 1Tx32Rx head coil (Figure 2A) is very inhomogeneous (central brightening demonstrated by the black ROI). This can be compared quantitatively by the standard deviation of the flip angle in the black, blue and white dotted ROIs (Figure 2A,C). In the blue ROI (Figure 2A,C) comparable mean flip angles could be achieved, which leads to comparable mean SNR in the white central ROIs (Figure 2B,D).

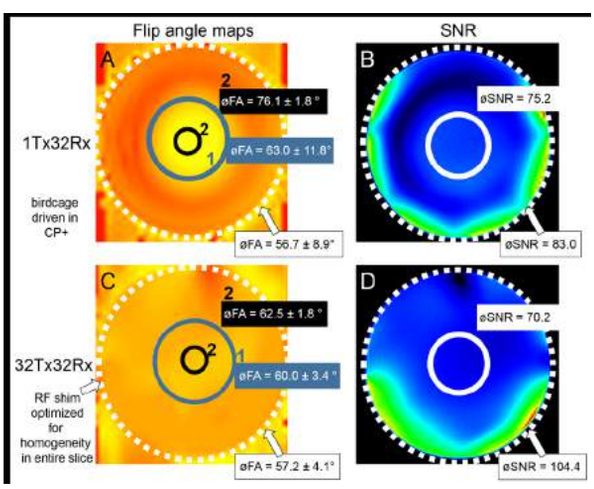

Figure 2: Transversal phantom measurements comparing the 1Tx32Rx head coil (A,B) and the 32Tx32Rx head coil (C,D). Comparable mean (ø) flip angles (A,C) are achieved in the entire slice (white dotted circle) and in the blue ROI. Consequently, the mean SNR in the white central ROI (B,D) for both coils is also approximately comparable. Higher SNR is achieved with the 32Tx32Rx coil when the entire slice is evaluated (B,D). Please note the clearly improved homogeneity of the dedicated RF shim (C) provided by the 32Tx32Rx head coil compared to the very inhomogeneous excitation of the CP+ mode generated by the birdcage of the 1Tx32Rx coil (A).

The evaluation of the entire transversal slice (white dotted circles in Figure 2B,D) results in a higher SNR of 104.4 for the 32Tx32Rx coil compared to 83.0 for the 1Tx32Rx coil. This corresponds to an SNR increase of 26% for the 32Tx32Rx coil. First MR imaging results in a melon (head) and stack of pineapple slices (neck) at 7T in transversal (Figure 3A), sagittal (Figure 3B), and coronal (Figure 3C) orientation were acquired using a 3D FLASH gradient echo sequence with 1 mm isotropic resolution, a TR/TE of 12/4.08 ms, and a total acquisition time of TA = 3 min 22 sec. These first experiments demonstrate the large field-of-view the 32Tx32Rx coil can cover.

Conclusion

The presented 32Tx32Rx head coil shows quite homogeneous excitation in preliminary investigations with static RF shimming and, depending on the ROI used for the evaluation, increased SNR in comparison to a commercial 1Tx32Rx coil. First MR imaging results in phantoms and fruits indicate the coverage of the human head as well as the neck. In-vivo brain/neck imaging and evaluation will start as soon as the ongoing safety evaluation of the RF coil is completed. Further steps will include the evaluation of more advanced pTx techniques like selective volume excitation.

References: 1. Pohmann R, Speck O, Scheffler K. Signal-to-Noise Ratio and MR Tissue Parameters in Human Brain Imaging at 3, 7, and 9.4 Tesla Using Current Receive Coil Arrays. Magn Reson Med 2016;75(2):1–9. 2. Orzada S, Bitz AK, Gratz M, Johst S, Shooshtray S, Völker MN, Rietsch SH, Flöser M, Abuelhaija A, Oehmigen M, et al. A 32-channel transmit system add-on for 7 Tesla body imaging. Proc Intl Soc MRM 25 2017. p. 1219. 3. Mao W, Smith MB, Collins CM. Exploring the limits of RF shimming for high-field MRI of the human head. Magn Reson Med 2006;56(4):918–22. 4. Katscher U, Börnert P, Leussler C, van den Brink JS. Transmit SENSE. Magn Reson Med 2003;49(1):144–50. 5. Brunheim S, Gratz M, Johst S, Bitz AK, Fiedler TM, Ladd ME, Quick HH, Orzada S. Fast and accurate multi-channel B1+ mapping based on the TIAMO technique for 7T UHF body MRI. Magn Reson Med 2018;79(5):2652–64.

The research leading to these results has received funding from the European Research Council under the European Union's Seventh Framework Programme (FP/2007-2013) / ERC Grant Agreement n. 291903 MRexcite, and DFG grant KO5341/1-1.

The contribution of the cerebellum to extinction: intrinsic mechanisms and cerebello-cerebral interactions.

A fundamental ability of the brain is to learn new stimulus-response associations, including motor, cognitive, emotional and autonomic responses. Equally important, the brain is also able to extinguish previously learned associations if no longer needed. There is good evidence that the cerebellum contributes to the acquisition and retention of new associations in these different domains (Timmann et al., 2010). Classical eyeblink conditioning has been studied in greatest detail and is well known to depend on the integrity of the cerebellum (Gerwig et al., 2003). Based on current concepts of cerebellar function, the cerebellum learns to predict correctly the relationship between the conditioned and unconditioned stimuli (CS and US) and to elicit a precisely timed conditioned response (CR). There

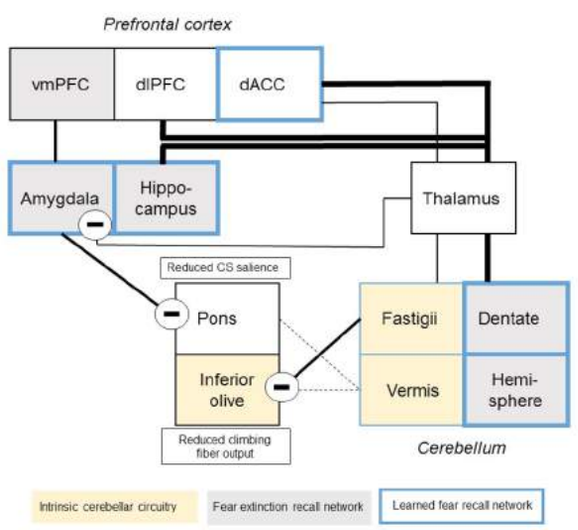

Figure 1) Simplified schematic diagram of the proposed role of the cerebellum in the brain network of extinction of conditioned fear (Steiner et al. Cerebellum 2018)

is also evidence that the cerebellum contributes to the acquisition and retention of conditioned fear responses (Machke et al., 2002). Although studied in less detail, the cerebellum has been found to contribute to the extinction of conditioned eyeblink responses (Thürling et al., 2015). We propose that the cerebellum is equally involved in the extinction of conditioned fear responses. Intrinsic cerebellar mechanisms, cerebello-cortical interactions and direct interactions between the cerebellum and amygdala may contribute to extinction. We will address these questions in a series of 7T fMRI experiments. Our work is performed as part of the Collaborative Research Center SFB1280 Extinction Learning (speaker: Onur Güntürkün, Ruhr University Bochum; co-speaker: Dagmar Timmann).

The overarching aim of our project is to provide evidence that the cerebellum has to be included as part of the brain network subserving extinction of conditioned fear. We propose that the cerebellum contributes to different aspects of extinction, and that different cerebellar areas are likely involved. Our proposed model of cerebellar involvement in extinction is based on four hypotheses (see also Fig. 1):

Hypothesis 1. Based on findings in eyeblink conditioning we predict that learned fear associations are at least partly reversed within the cerebellum during extinction. The inferior olive likely plays an important role. Vermis and fastigial nuclei are proposed to contribute to extinction of learned autonomic fear responses, and the posterolateral hemispheres and the dentate nuclei to extinction of higher emotional/cognitive fear responses.

Hypothesis 2. In addition to bidirectional learning within the cerebellum, it appears likely that there is also learned inhibition, which contributes to extinction of fear-related associations within the cerebellum. In accordance with proposals on extinction of conditioned eyeblink responses by others, we hypothesize that the cerebellum is under the inhibitory control of the known cerebral fear extinction network.

Hypothesis 3. Extinction is known to be context-dependent. Based on known functional and (partly mapped) structural

cerebello-cerebral connections, we hypothesize that the cerebellum modulates context-related processes within the hippocampus, and/or initial shifts of attention to changes in context within the dorsolateral prefrontal cortex (PFC). Because cerebello-cerebral connections are best known for the posterolateral cerebellum, the posterolateral hemisphere and its output nuclei, the dentate nucleus, may be primarily involved.

Hypothesis 4. Finally, we propose that there is also a more direct interaction between the cerebellum and the amygdala during extinction of learned fear. The cerebellar nuclei are proposed to inhibit the amygdala during extinction.

The high signal-to-noise ratio (SNR) at 7T ultrahigh field (UHF) will be exploited to study the proposed mechanisms within the cerebellum underlying extinction of learned fear. 7T UHF allows performing imaging studies at the level of the dentate and interposed nuclei (Ernst et al., 2017). One important aim of our project is to extend our previous work to the level of the fastigial nuclei and inferior olive. We want to provide evidence that not only the vermal cortex, but also the fastigial nuclei and the inferior olive play a role in acquisition and extinction of autonomic learned fear responses in humans. We expect that there is additional activation of the posterolateral cerebellar hemisphere and the dentate nucleus related to higher emotional and cognitive aspects of learned fear. We propose that the cerebellar vermis and posterolateral cerebellar hemispheres play different roles in extinction of autonomic fear responses. The vermis is expected to be primarily involved in association and extinction of learned autonomic fear responses, and the posterolateral hemisphere in context-related processes.

We were able to establish a fear conditioning setup in the 7T MR scanner including electrical stimulation of the hand (as US), presentation of visual stimuli (as CS+ und CS-) and recording of skin conductance responses (SCR), pulse and breathing rate. Whereas SCR, pulse and breathing rate are collected with commercially available MR-safe systems, a cable for the application of the electrical stimuli had to be custom-built. We are able to draw on the comprehensive preparatory work of Marcel Gratz, a postdoc in Harald Quick's group, who designed a highly resistive 7T MR conditional cable (10 kΩ/m) using MR compatible, non-magnetic SMD-resistors, and had performed extensive safety tests in the past. Pilot 7T MRI data in 23 healthy subjects shows significant fMRI activation of the fastigial and dentate nuclei related to the unconditioned stimulus (US), that is painful stimulation of the hand (Fig. 2). Fear conditioning studies in healthy human subjects with and without context changes are currently ongoing. A deeper understanding of the cerebellar contribution to the fear extinction network will provide further insight in the long proposed involvement of the cerebellum in emotional functions in health and disease.

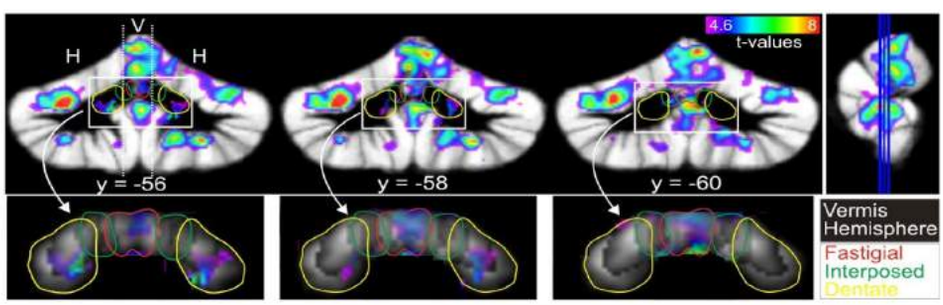

Figure 2: Pilot 7T MRI data in 23 healthy subjects showing significant fMRI activation ($p < 0.05$, permutation corrected) of the fastigial and dentate nuclei related to the US.

References: 1. Ernst TM, Thürling M, Müller S, Kahl F, Maderwald S, Schlamann M, Boele HJ, Koekkoek SKE, Diedrichsen J, De Zeeuw CI, Ladd ME, Timmann D. Modulation of 7 T fMRI signal in the cerebellar cortex and nuclei during acquisition, extinction, and reacquisition of conditioned eyeblink responses. Hum Brain Mapp. 2017;38:3957-397. 2. Gerwig M, Dimitrova A, ..., Timmann D (2003) Comparison of eyeblink conditioning in patients with superior and posterior inferior cerebellar lesions. Brain. 126:71-94. 3. Maschke M, Schugens M, Kindsvater K, Drepper J, Kolb FP, Diener HC, Daum I, Timmann D (2002) Fear conditioned changes of heart rate in patients with medial cerebellar lesions. J Neurol Neurosurg Psychiatry. 72:116-8. 4. Steiner KM, Gisbertz Y, Chang DI, Koch B, Uslar E, Claassen J, Wondzinski E, Ernst TM, Göricke SL, Siebler M, Timmann D. (2018) Extinction and renewal of conditioned eyeblink responses in focal cerebellar disease. Cerebellum. [Epub ahead of print] 5. Thürling M, Kahl F, Maderwald S, Stefanescu RM, Schlamann M, Boele HJ, De Zeeuw CI, Diedrichsen J, Ladd ME, Koekkoek SK, Timmann D (2015) Cerebellar cortex and cerebellar nuclei are concomitantly activated during eyeblink conditioning: a 7T fMRI study in humans. J Neurosci. 35:1228-39. 6. Timmann D, Drepper J, Frings M, et al. (2010) The human cerebellum contributes to motor, emotional and cognitive associative learning. A review. Cortex. 46:845-57.

Funded by Collaborative Research Center (Sonderforschungsbereich) SFB 1280 Extinction Learning / Project A05.

Laminar fMRI with T2-prepared multi-echo FLASH

The Emmy-Noether funded research group of Dr. Koopmans is interested in methodical developments to improve high resolution data acquisition and data analysis techniques for laminar functional magnetic resonance imaging (fMRI). Highfield systems, such as the 7T scanner at the Erwin L. Hahn Institute, deliver the signal-to-noise ratio needed to push the temporal and spatial resolution for layer resolved fMRI.

One goal of high resolution fMRI is to examine signal changes at the level of cortical laminae. The cortex can be subdivided into six histological layers, with different functions. For example, layer 4 is typically associated with bottom-up input from brain regions lower in the hierarchy, whereas deeper layers receive feedback input from higher brain regions. Therefore, imaging the brain at a sub-millimeter resolution with laminar fMRI techniques can provide unique insights into the directionality of information processing in the brain[1].

The vast majority of fMRI studies use T_2*-weighted echo-planar imaging (EPI) to be as sensitive as possible to the subtle signal changes induced by functional activity. However, this sensitivity benefit comes at the price of specificity: venous signal relatively far away from the site of neuronal activity is a strong contributor to the T_2* BOLD signal (see Figure 1). T_2-weighted sequences (note the absence of the * sign) have superior specificity as they are less sensitive to these larger veins. Unfortunately, it is hard to perform T_2-weighted experiments due to technical as well as biophysical limitations.

T_2-prepared sequences[2] have recently been proposed to perform T_2-weighted fMRI to reduce the sensitivity to draining vein effects. We investigated the feasibility of a T_2-prepared, multi-echo

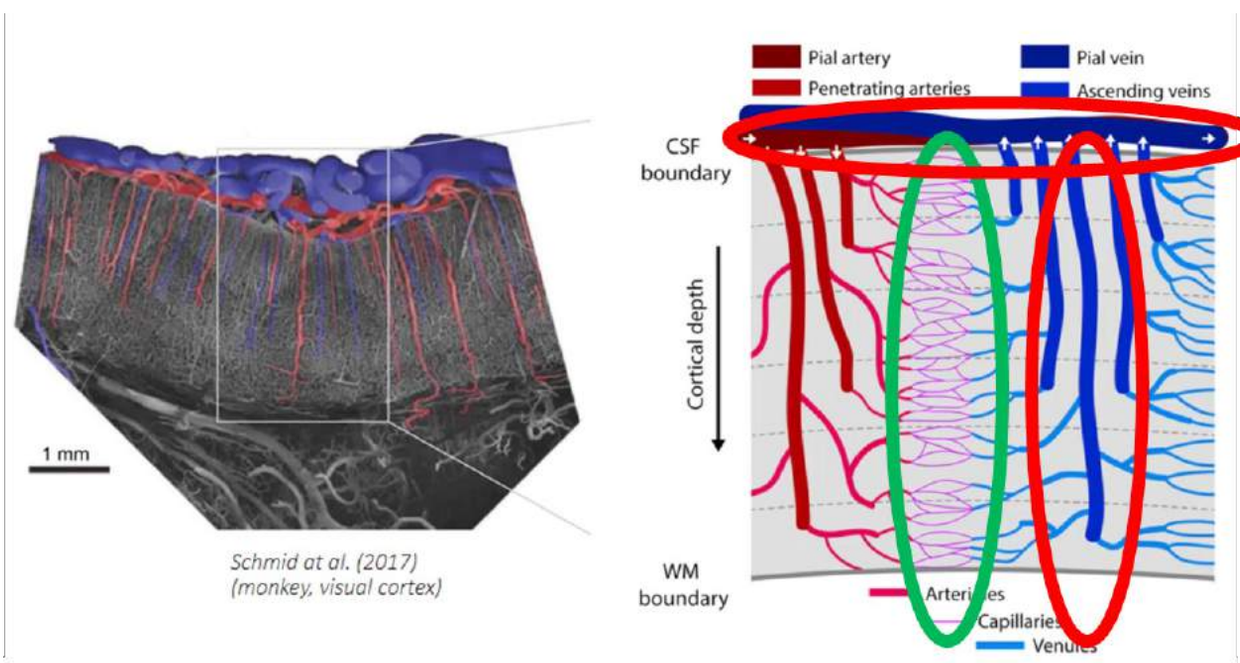

Figure 1: In order to be able to discern cortical depth dependent signal, ideally the experiment would only be sensitive to activation effects measured in the capillaries (green oval). In standard, T_2*-weighted, fMRI sequences we are also sensitive to effects in the larger draining veins (red ovals), which reduce the specificity. To illustrate: blood from the capillaries in the middle layers travels towards the surface in the ascending veins (blue vertical vessels in the red oval), passing through the layers above. This can give a false impression that the neuronal effect is also present in the superficial layers. T_2-weighted sequences are less sensitive to the larger vessels in the red ovals than T_2*-weighted ones and can thus potentially increase the spatial specificity of laminar fMRI.

Viktor Pfaffenrot, Peter J. Koopmans

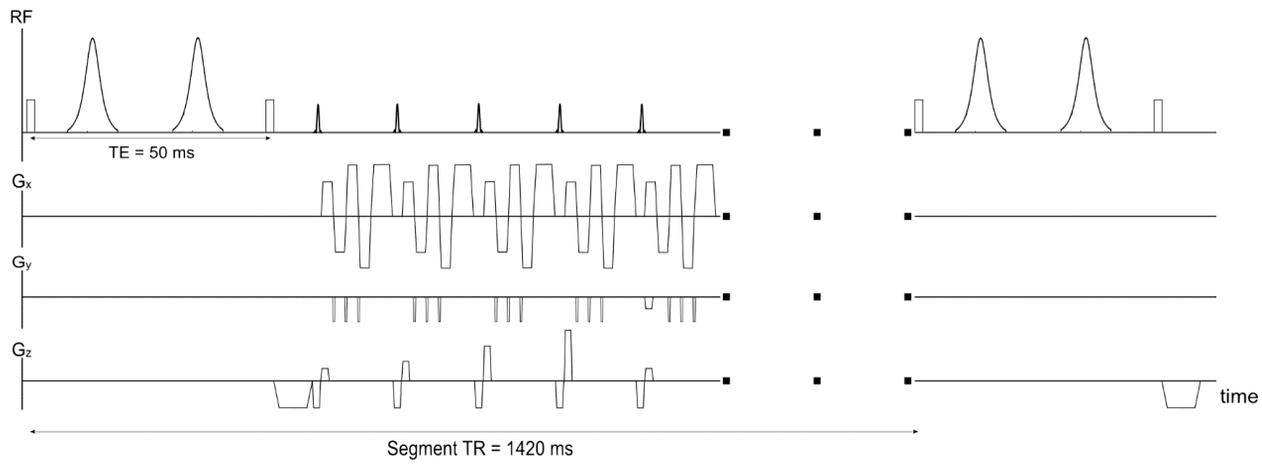

Figure 2: Schematic of the T_2-prep multi-echo 3D FLASH sequence. A multi-echo FLASH readout follows a T_2-prep module of 50 ms duration. Four echoes are acquired per shot. The Y-gradient blips between echoes shift improve the joint-reconstruction process. To minimize T_1-relaxation effects after the T_2-prep module both phase encoding axes are acquired in a center-out scheme. In addition, the partition encoding loop (Gz) is 8-fold segmented leading to a segment TR of 1.42 s.

3D FLASH sequence in a flickering checkerboard experiment targeting the visual cortex for laminar fMRI.

Methods

A schematic of the used sequence is shown in Figure 2. The echo time of the T_2-prep module was 50 ms for optimal sensitivity in gray matter (GM) (T_2 = 50 ms @ 7 T). This module attenuates the longitudinal magnetization that is available for the FLASH readout following it. As venous blood has a very short T_2[3] the blood signal is expected to be close to fully attenuated by the T_2-prep module. As the FLASH multi-echo readout has echo times ranging from 2.6 ms to 8.8 ms, the extravascular contribution is expected to be attenuated as well, to approximately 25 % - 60 % of its maximum response at the conventionally used echo time close to the gray matter T_2* of 30 ms. Taken together, the expectation is that the T_2-weighting maximizes sensitivity to capillary changes in GM, whilst suppressing/attenuating unwanted venous effects.

A 256x256x32 matrix was acquired per echo. TEs were 2.88 ms, 4.84 ms, 6.8 ms, and 8.76 ms. TR was 11.2 ms. We used an undersampling factor of 8 in the phase-encode dimension, but shifted the sampling patterns of the echoes w.r.t. each other to aid the joint reconstruction process[4]. This method uses all echoes to inform the reconstruction of a single one resulting in lower g-factors. The volume TR was 11.4 seconds. As T_1 relaxation would certainly nullify the T_2 preparation over such a long time, 8-fold segmentation was applied, resulting in 1.42 seconds of acquisition time per segment. To further reduce T_1-relaxation artefacts, the encoding was performed center-out. Activity was induced using a flashing checkerboard in a 40-minute run in a single subject. Structural data (mprage) were processed in FreeSurfer to be able to perform cortical depth sampling in the functional data. Standard fMRI processing steps (registration, temporal filtering, etc.) were carried out using SPM12.

Results

The laminar profiles of 'Checkerboard ON-OFF' are shown in Figure 3a for the four echoes. We discuss two noteworthy depths here:
1) Deep in GM (red arrow in Figure 3a), the activity is relatively independent of TE. An extravascular effect (caused by pial/ascending veins) would have shown an approximately linear increase with TE but this is absent. Instead, the signal change is likely dominated by GM T_2 changes, which is the goal of T_2-prep fMRI.
2) There is a very large signal change at the pial surface, which seems to be caused by veins as shown in the overlay image in Figure 4. Multiple mechanisms

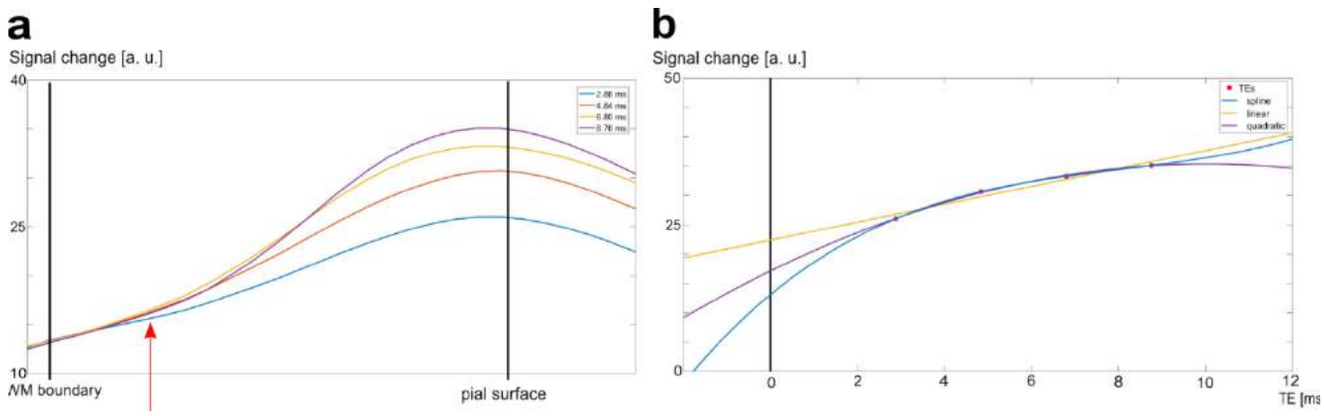

Figure 3: A) Layer profiles for each individual TE. Signal changes increase towards the pial surface for every echo time and also increase as a function of TE. The red arrow indicates activity change in deep GM layers where the echo time dependence is much less apparent. B) Signal change as a function of TE at the pial surface. Even with very liberal curve fits, signal change is not zero as TE = 0 ms (black line). This hints at an intravascular signal contribution, likely due to elongated blood T_2 during activity.

could perhaps explain this: (A) An extravascular effect in the cerebrospinal fluid (CSF). The diffusion in CSF is much larger than in tissue and therefore the regime in which dephasing cannot be refocused with an 180 degree pulse is much wider. However at TE = 0, the change should be zero, and even very liberal curve fits (shown in Figure 3b) are not able to intersect the y-axis anywhere near 0. (B) T_1-relaxation could cause venous blood signal to reappear during the FLASH readout, which would then result in high T_2*-weighted intravascular signal changes (despite the center-out encoding). However, here too, the extrapolation through the origin seems unlikely. (C) Blood T_2 in an activated state could be much higher than expected. In this case, there is a difference in ON vs OFF, prior to the FLASH readout resulting in the y-axis offset. (D) Inflow of 'fresh' blood (i.e. blood which did not experience one or more former RF pulses in a repetitive sequence) may cause increased longitudinal magnetization which leads to the same intravascular signal behavior as in (B).

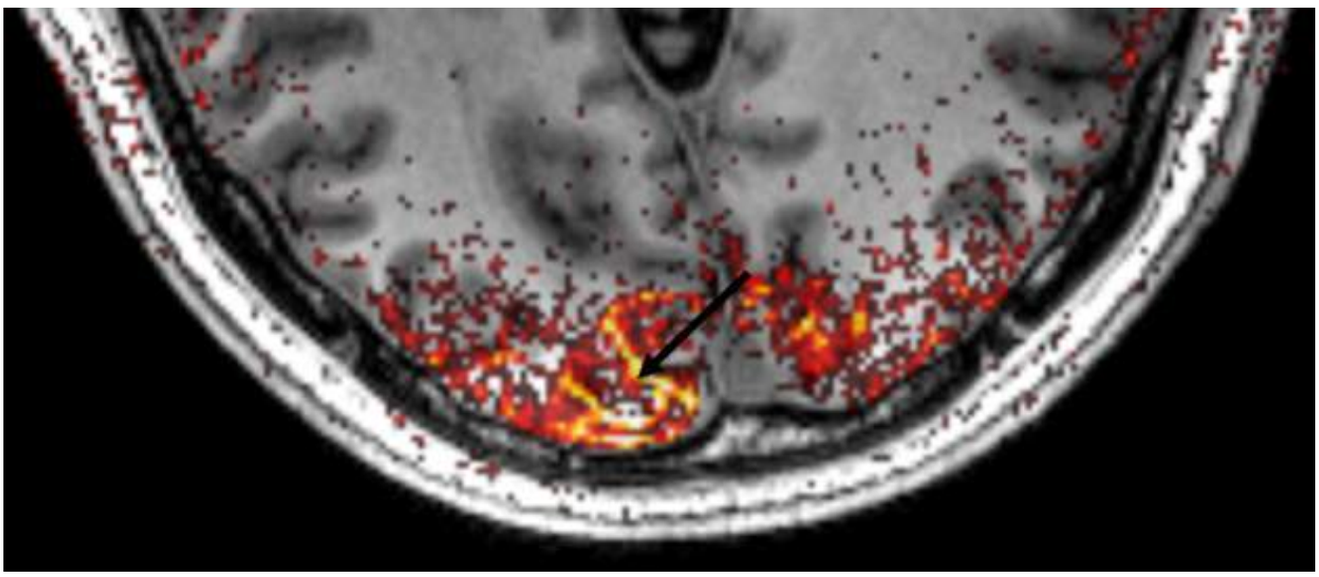

Figure 4: fMRI activity (maximum intensity projection over a few slices) overlaid on an anatomical slice. A pial vein (black arrow) can be seen indicating intravascular contributions to the T_2-weighted functional data.

Discussion

The results suggest that in the deep layers the T_2-prep method works as intended: the signal changes barely vary with echo time, indicating they are likely dominated by the T_2 weighting from the T_2-prep module (as opposed to being dominated by T_2*). In the higher layers, there are still signal contributions that do vary with echo time. We suspect that this is intravascular blood signal: perhaps, upon activation, the elongation of the T_2 of venous blood is large enough to violate our assumptions that the blood signal contribution has become negligible. We are currently investigating this by repeating the measurements with different values of the T_2-prep echo time, and by suppressing intravascular blood signal using diffusion gradients. Combined, we will try and assess the contributions of the ascending veins. This is important because the unwanted contribution of the ascending veins cannot be addressed by increasing the spatial resolution of the sequence further, so we need to do the next best thing: study its extent and impact on laminar fMRI.

References: 1. Kok et al. Current Biology 2016; 26:371-76. 2. Hua et al. MRM 2014; 72:1530-40. 3. Uludag et al. NeuroImage 2009; 48:150-65. 4. Bilgic et al. MRM 2018; 80:619-632.

The research leading to these results has received funding from the DFG grant KO5341/1-1.

Laminar Specific fMRI Reveals Directed Interactions in Distributed Networks During Language Processing

Top-down and bottom-up information streams are integral to brain function but notoriously difficult to measure non-invasively. Laminar resolution, functional magnetic resonance imaging (lfMRI) is a promising noninvasive technique with the potential to distinguish top-down and bottom-up signal contributions to the hemodynamic response.

The brain exhibits a layered structure whereby neurons are arranged in a layered, or laminated, structure. This structure has consequences for brain function as information which comes from higher or lower brain regions is distinguishable by virtue of layer specific synaptic connections preferred by the different information streams. By dissociating these streams, we show that it is possible to determine the hierarchical relationship between brain regions and therefore the directed flow of information through brain networks.

There are clear motivations to identify directed functional signal pathways throughout the brain. Directed connectivity methods are useful to discover brain networks, to inform parcellations of the brain, to increase the context of other parcellation methods, and, ultimately, to better understand the nature of large scale neural computation. More immediately, directed measurements could help resolve difficult questions in cognitive neuroscience. The study of language can be used as a concrete example.

This project concerned the processes and brain regions supporting word reading. Word reading is known to engage brain regions in the left occipitaltemporal sulcus (lOTS) and the left temporal cortex. The experimental question was whether connectivity between the lOTS and left temporal regions is best characterized by bottom-up or top-down signaling between the regions. To answer

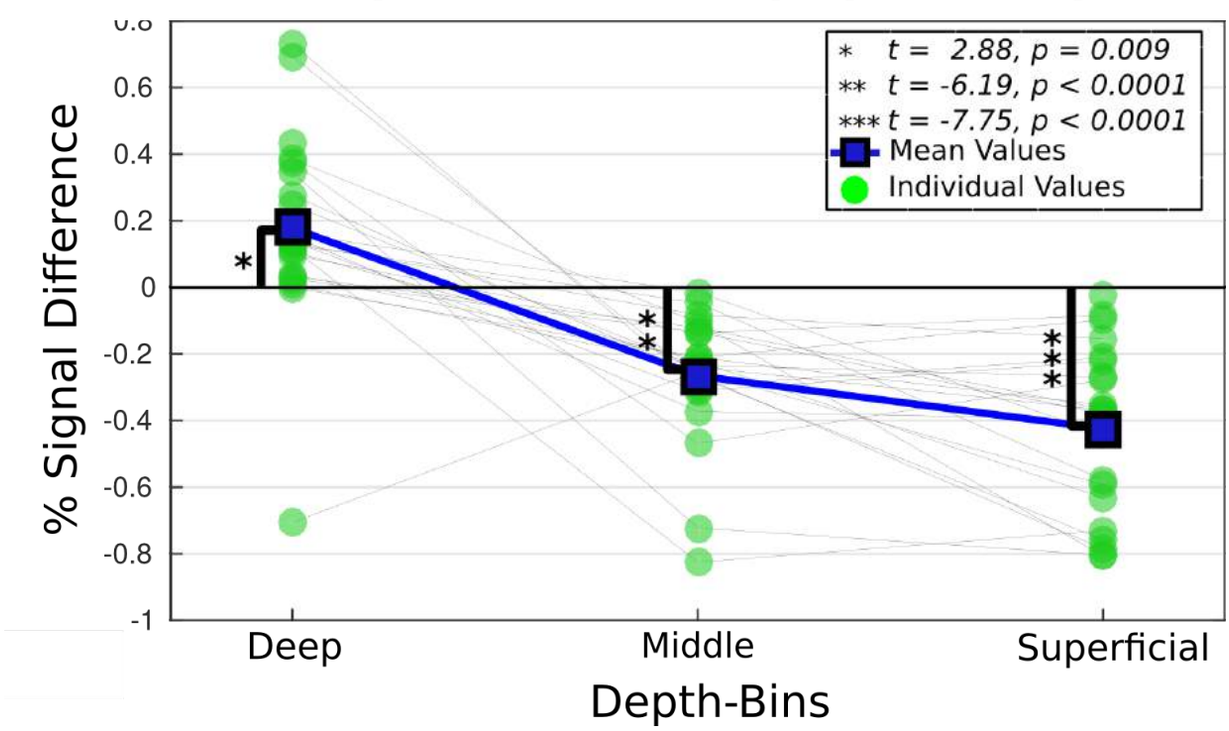

Figure 1: The difference in percent signal change between words and pseudo-words is shown by depth for all participants. Significance bars relate to t-statistics computed on the difference from 0 (n = 22).

this question, we utilized a word reading paradigm in which participants read words, pseudo-words, and strings of characters taken from a fabricated false-font, while scanning at high spatial resolution, using 3D gradient-echo BOLD EPI. 22 healthy volunteers were imaged. We predicted that words would elicit a stronger top-down response relative to pseudo-words and that the overall signal would be reduced for words compared to pseudo-words. Based on known properties of laminar anatomy, the increased top-down signal was expected to target the deeper portions of the lOTS.

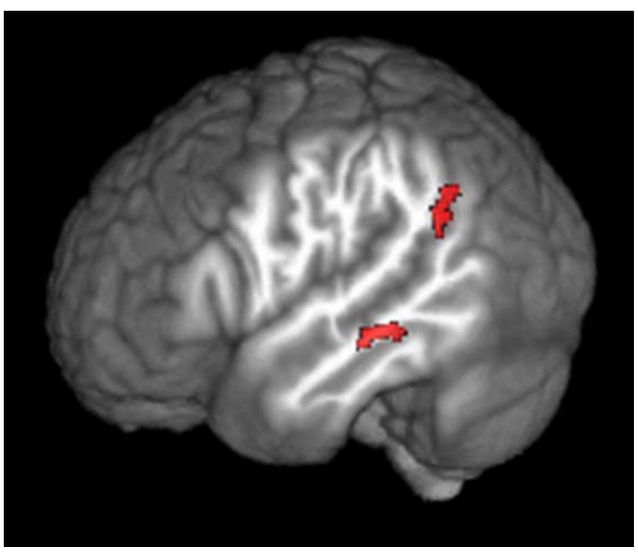

Figure 2: Words against pseudo-words gPPI results for the deep bin. Shown in red: the deep bin preferentially targets left lateralized, language critical regions during word reading. p = 0.001, α = 0.05, n = 21

Another primary goal of this project was to demonstrate that these signal streams preserve source information and can be used to identify directed networks. Using the laminar measurement, we identified distinct distributed networks corresponding to top-down and bottom-up signal pathways which targeted the lOTS during word reading.

The results of this project show that that reading words compared to pseudo-words increased the top-down BOLD signal observed in the deep layers of the lOTS (Figure 1), that the deep bin signal increases accompanied signal decreases in the middle and superficial bins (Figure 1), that increases in deep bin signal predicted decreases in the middle bin for words but not for pseudo-words, and that the depth-dependent signal demonstrated unique connectivity patterns with other brain regions in the language network (Figure 2), thereby establishing directionality of interaction within the reading network.

These discoveries establish lfMRI for the noninvasive assessment of directed connectivity during task performance, something that will have wide-reaching implications for cognitive neuroscience research.

Current Grants

T. W. Scheenen, J. J. Fütterer, F. Witjes, M. Sedelaar, M. Maas, J. O. Barentsz, D. W. J. Klomp, H. H. Quick: Radboudumc: **A personalized image-based assessment of metastatic potential of prostate cancer** (2018-2021)

In this grant the assessment of the aggressiveness of localized prostate cancer is correlated and validated with early detection of the first metastases of the disease.

N. Axmacher, D. Timmann-Braun, H. H. Quick: DFG: **Focus group Neuroimaging: Extinction network connectivity across learning paradigms** (2017-2021)

In this joined project between PIs of the RUB and UKE, metaanalyses will be performed of fMRI data acquired in SFB1280. The main aim is to systematically investigate structural and functional extinction network connectivity across different learning paradigms and subject populations.

D. Timmann-Braun, H. H. Quick: DFG: **The contribution of the cerebellum to extinction: intrinsic mechanisms and cerebello-cerebral-interactions** (2017-2021)

The main aim of the project is to provide experimental evidence that the cerebellum has to be included as part of the neural circuitry underlying extinction of conditioned fear responses.

P. Koopmans: DFG Emmy Noether Programme – Independent Junior Research Group: **Functional Magnetic Resonance Imaging of cortical layers to measure directionality of information flow in brain networks for pain** (2016-2021)

Dr. Koopmans proposal focuses on the development of a high-resolution fMRI technique to improve understanding of how the brain processes pain.

T. W. Scheenen, H. H. Quick, J. O. Barentsz: Radboudumc: **Nanotechnology at ultra-high magnetic field: towards in vivo detection of small lymph node metastases with MRI** (2016–2020)

In this project the highest sensitivity of 7T to detect in vivo small lymph node metastases will be validated with histopathology of resected tissues in patients with rectal cancer.

M. E. Ladd, H.H. Quick, O. Speck: DFG: **German ultra-high field imaging (GUFI)**, Core Facility (2016-2019)

Aim of this project is to maintain and expand a nationwide network of UHF-MRI sites.

D. Timmann (PI), M. E. Ladd, A. Deistung (PI), J. Reichenbach: DFG: **In vivo assessment of the cerebellum by novel MRI techniques and application to hereditary ataxias: morphological, pathoanatomical and clinical aspects** (2015-2018)

The aim of this collaboration project is to obtain deeper insight into the pathoanatomy of cerebellar nuclei in common forms of degenerative ataxias by using novel MRI techniques.

H. H. Quick, D. G. Norris: **SIEMENS Healthcare GmbH: Cooperation agreement 7T High Field MR imaging, Erwin L. Hahn Institute** (2015-2018)

This cooperation agreement encompasses sequence and 7T MRI application development as well as ELH-provided feedback of clinical experience using the pTX Array step 2.

D. G. Norris, P. Hagoort: NWO: **Language regions in Interaction: An investigation of directional connectivity in the human language system using laminar fMRI** (2014-2018)

This ambitious project will examine the interaction between temporal cortex, and Broca's area during language comprehension using event-related fMRI at 7T.

D. Norris, I. Tendolkar, M. Brand, J. Wiltfang, J. Schulz : Helmholtz-Gesellschaft: **Imaging and Curing Environmental Metabolic Diseases (ICEMED), Research Topic 4: Next generation CNS Imaging for metabolic disease** (2012-2018)

The primary goal of this project is to examine ways of improving cognitive deficits, particularly in episodic memory performance, in patients suffering from type 2 diabetes (T2DM).

Erwin L. Hahn Lecture 2018

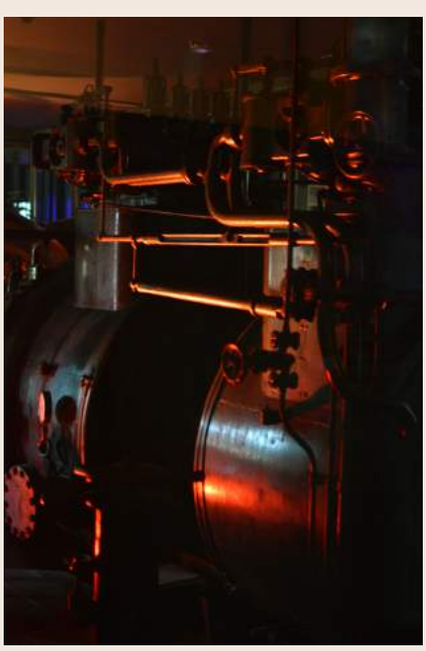

Personnel and Organisational Structure at ELH

Directorate / Principal Investigators

Managing Director/PI
Prof. Dr. David G. Norris

Director/PI
Prof. Dr. Matthias Brand
Prof. Dr. Harald H. Quick

PI
Prof. Dr. Ulrike Bingel
Dr. Tom W. J. Scheenen

Associated PIs
Dr. Peter J. Koopmans
Prof. Dr. Mark E. Ladd
Prof. Dr. Dagmar Timmann-Braun

Management

Administrative Director
Judith Kösters

Staff Scientist
Dr. Oliver Kraff
Dr. Stefan Maderwald

Radiographer
Lena Schäfer

Assistance
Sigrid Radermacher
Susanne Hinsenkamp

Public Relations
Stefanie Zurek

Scientists

MSc. Stephanie Antons
Dr. Giorgi Batsikadze
MSc. Jacob Bellmund
MSc. Sascha Brunheim
MSc. Guillermo Carbonell
Dr. med. Jens Claaßen
Dr. Andreas Deistung
Dr. med. Cornelius Deuschl
Dipl.-Phys. Thomas Ernst
Dr. med. Oliver Gembruch
Dr. rer. nat. Marcel Gratz
MSc. Donghyun Hong
MSc. Irati Markuerkiaga
Dr. Silke M. Müller
Dr. Stephan Orzada
MSc. Viktor Pfaffenrot
Dr. Bart Philips
MSc. Stefan H. G. Rietsch
Dipl.-Psych. Christoph Ritter
MSc. Katrin Scharmach
Dr. Jennifer Schulz
MSc. Daniel Sharoh
MSc. Tobias Spronk
Dr. Emma Sprooten
Dr. Katrin Starcke
Dr. med. Rutger Stijns
Prof. Dr. med. Indira Tendolkar
MSc. Jan-Willem Thielen
Dr. Patrick Trotzke
Dipl.-Ing. Maximilian Völker

Students

Nora Schulz
Katharina Schröder
Jessica Kohl
Larissa Meding

New in 2018

Larissa Meding
Tobias Spronk

Left in 2018

Sascha Brunheim
Donghyun Hong
Jessica Kohl
Lena Schäfer
Katharina Schröder
Nora Schulz

Participation at ISMRM 2018 in Paris, France

Sascha Brunheim: 16-channel pTx body MRI for reduced field of view lumbar spine and kidney imaging at 7 Tesla

Marcel Gratz: From phantoms to patients: Paving the way for MRF in clinical practice

Donghyun Hong: Implications of magnetic susceptibility difference between grey and white matter for spectroscopy quantification at 7T.

Donghyun Hong: Optimal phased-array signal combination from separate coil elements for GABA quantification at 7T

Oliver Kraff: Experience with 7 Tesla MRI of human subjects with passive implants and tattoos: an update

Mark Ladd: *Talk* ,"The payoff for the pain" in the Educational Course "Primer for Ultrahigh Field MRI"

Mark Ladd: Co-Organizer of the Member-Initiated Symposium "MRI in Radiation Therapy"

Maike Lindemann: Radiotracer dose reduction in 18F-FDG whole-body PET/MR: Effects on image quality and quantification

Stephan Orzada: Transmit Arrays & Circuitry for UHF Body Imaging

Stefan Rietsch: A 16-channel Rx-only radiofrequency coil for MR spine imaging at 7T

Rutger Stijns: The workflow for the validation of USPIO-enhanced MRI for the detection of lymph node metastases in rectal cancer

Publications on 7T MRI

Brunheim, S.; Gratz, M.; Johst, S; Bitz, A.K.; Fiedler, T.M.; Ladd, M.E.; Quick, H.H.; Orzada, S. Fast and accurate multi-channel B1+ mapping based on the TIAMO technique for 7T UHF body MRI. (2018) *Magnetic Resonance in Medicine*. 79(5):2652-2664.

Fiedler, T.M.; Ladd, M.E.; Bitz, A.K. SAR Simulations & Safety. (2018) *Neuroimage*. 168:33-58. doi: 10.1016/j.neuroimage.2017.03.035.

Goebel, J.; Nensa, F.; Schemuth, H.P.; Maderwald, S.; Schlosser, T.; Orzada, S.; Rietsch, S.H.G.; Quick, H.H.; Nassenstein. K. Feasibility of aortic valve planimetry at 7 T ultrahigh field MRI: Comparison to aortic valve MRI at 3 T and 1.5 T. (2018) *European Journal of Radiology*. 5: 159–164

Hong, D.; Asten, J.J.Av.; Rankouhi, S.R.; Thielen, J. W.; Norris, D.G. (2018) Implications of the magnetic susceptibility difference between grey and white matter for single-voxel proton spectroscopy at 7 T. (2018) *Journal of Magnetic Resonance*. 297:51-60. doi: 10.1016/j.jmr.2018.10.007

Kording, F.; Ruprecht, C.; Schoennagel, B.; Fehrs, K.; Yamamura, J.; Adam, G.; Goebel, J.; Nassenstein, K.; Maderwald, S.; Quick, H.H.; Kraff, O. Doppler ultrasound triggering for cardiac MRI at 7T. (2018) *Magnetic Resonance in Medicine*. 80(1):239-247.

Laader, A.; Beiderwellen, K.; Kraff, O.; Maderwald, S.; Ladd, M.E.; Forsting, M.; Umutlu, L. Non-enhanced versus low-dose contrast-enhanced renal magnetic resonance angiography at 7 T: a feasibility study. (2018) *Acta Radiologica*. 59(3):296-304. doi: 10.1177/0284185117718399.

Ladd, M.E.; Bachert P., Meyerspeer, M.; Moser, E.; Nagel, A.M.; Norris, D.G.; Schmitter, S.; Speck, O.; Straub, S.; Zaiss, M. Pros and cons of ultra-high-field MRI/MRS for human application. (2018) *Progress in Nuclear Magnetic Resonance Spectroscopy* 109:1-50, 2018.

Ladd, M.E. The quest for higher sensitivity in MRI through higher magnetic fields. (2018) *Zeitschrift für medizinische Physik*. 28(1):1-3.

Marques, J.P.; Norris, D.G. How to choose the right MR sequence for your research question at 7T and above? (2018) *Neuroimage*. 168:119-140. doi: 10.1016/j.neuroimage.2017.04.044.

Matsushige, T.; Kraemer, M.; Sato, T.; Berlit, P.; Forsting, M.; Ladd, M.E.; Jabbarli, R.; Sure, U.; Khan, N.; Schlamann, M.; Wrede, K.H. Visualization and Classification of Deeply Seated Collateral Networks in Moyamoya Angiopathy with 7T MRI. (2018) *AJNR. American Journal of Neuroradiology*. 39(7):1248-1254. doi: 10.3174/ajnr.A5700

Noureddine, Y.; Kraff, O.; Ladd, M.E.; Wrede, K.H.; Chen, B.; Quick, H.H.; Schaefers, G.; Bitz, A.K. In vitro and in silico assessment of RF-induced heating around intracranial aneurysm clips at 7 Tesla. (2018) *Magnetic Resonance in Medicine*. 79(1):568-581. doi: 10.1002/mrm.26650.

Pfaffenrot, V.; Brunheim, S.; Rietsch, S.H.G.; Koopmans, P.J.; Ernst, T.M.; Kraff, O.; Orzada, S.; Quick, H.H. An 8/15-channel Tx/Rx head neck RF coil combination with region-specific B1+ shimming for whole-brain MRI focused on the cerebellum at 7T. (2018) *Magnetic Resonance in Medicine*. 80(3):1252-1265. doi: 10.1002/mrm.27125

Rietsch, S.H.G.; Orzada, S.; Maderwald, S.; Brunheim, S.; Philips, B.W.J.; Scheenen, T.W.J.; Ladd, M.E.; Quick, H.H. 7T ultra-high field body MR imaging with an 8-channel transmit/32-channel receive radiofrequency coil array. (2018) *Medical Physics.* 45(7):2978-2990. doi: 10.1002/mp.12931

Rietsch, S.H.G.; Orzada, S.; Bitz, A.K.; Gratz, M.; Ladd, M.E.; Quick, H.H. Parallel transmit capability of various RF transmit elements and arrays at 7T MRI.(2018) *Magnetic Reonance in Medicine.* 79(2):1116-1126. doi: 10.1002/mrm.26704.

Rohani Rankouhi, S.; Hong, D.; Dyvorne, H.; Balchandani, P.; Norris, D.G. MASE-sLASER, a short-TE, matched chemical shift displacement error sequence for single-voxel spectroscopy at ultrahigh field. (2018) *NMR in Biomedicine.* 31(7):e3940. doi: 10.1002/nbm.3940.

Suntharalingam, S.; Mladenov, E.; Sarabhai, T.; Wetter, A.; Kraff, O.; Quick, H.H.; Forsting, M.; Iliakis, G.; Nassenstein, K. Abdominopelvic 1.5-T and 3.0-T MR Imaging in Healthy Volunteers: Relationship to Formation of DNA Double-Strand Breaks. (2018) *Radiology.* 288(2):529-535

Tran, L.; Huening, B.M.; Kaiser, O.; Schweiger, B.; Sirin, S.; Quick, H.H.; Felderhoff-Mueser, U.; Timmann, D. Cerebellar-dependent associative learning is impaired in very preterm born children and young adults. (2017) *Scientific Reports.* 7(1):18028. doi: 10.1038/s41598-017-18316-8.

van de Bank, B.L.; Maas, M.C.; Bains, L.J.; Heerschap, A.; Scheenen, T.W.J. Is visual activation associated with changes in cerebral high-energy phosphate levels? (2018) *Brain Structure & Function* . 223(6):2721-2731. doi: 10.1007/s00429-018-1656-7

van Veenendaal, T.M.; Backes, W.H.; Tse, D.H.Y.; Scheenen, T.W.J.; Klomp, D.W.; Hofman, P.A.M.; Rouhl, R.P.W.; Vlooswijk, M.C.G.; Aldenkamp, A.P.; Jansen, J.F.A. High field imaging of large-scale neurotransmitter networks: Proof of concept and initial application to epilepsy. (2018) *NeuroImage: Clinical* 19, 47-55. doi: 10.1016/j.nicl.2018.04.006

Book Chapter:

Ladd, M.E.; Quick, H.H.; Bock, M.; Berger, M.; Breithaupt, M.; Nagel, A.M.; Bitz, A.K.; Komljenovic, D.; Laun, F.B.; Kuder, T.A.; Bachert, P.; Lanzman, R.S.; Wittsack, H.J. (2018) Magnetresonanztomographie und –spektroskopie [Magnetic resonance imaging and spectroscopy]. In: Schlegel, W.; Karger, C.P.; Jäkel, O. (eds) *Medizinische Physik [Medical physics]*, Springer Spektrum, Wiesbaden, 205-283

Awards

Sascha Brunheim: Gorter Award (2nd place) awarded by the German Chapter of the International Society for Magnetic Resonance in Medicine for his contribution "Parallele, 2D-selektive HF-Anregung der Wirbelsäule basierend auf B01TIAMO mit einem 32-Kanal Transceiver-System bei 7 Tesla."

Oliver Kraff: ISMRM Distinguished Reviewer Award (for Magnetic Resonance in Medicine)

Stephan Orzada: ISMRM Distinguished Reviewer Award (for Magnetic Resonance in Medicine)

Stephan Orzada: ISMRM "Outstanding Teacher Award" for his invited talk "Transmit Arrays & Circuitry for UHF Body Imaging."

Stefan H.G. Rietsch: Young Investigator Award awarded by the Deutsche Gesellschaft für Medizinische Physik (DGMP) for his contribution „Evaluation einer 8-Kanal-Sende/32-Kanal-Empfangsspule für die 7T MRT im Körper."

Mark E. Ladd: Election as President of the Deutsche Gesellschaft für Medizinische Physik (DGMP) [German Society for Medical Physics] in 2019-2020.

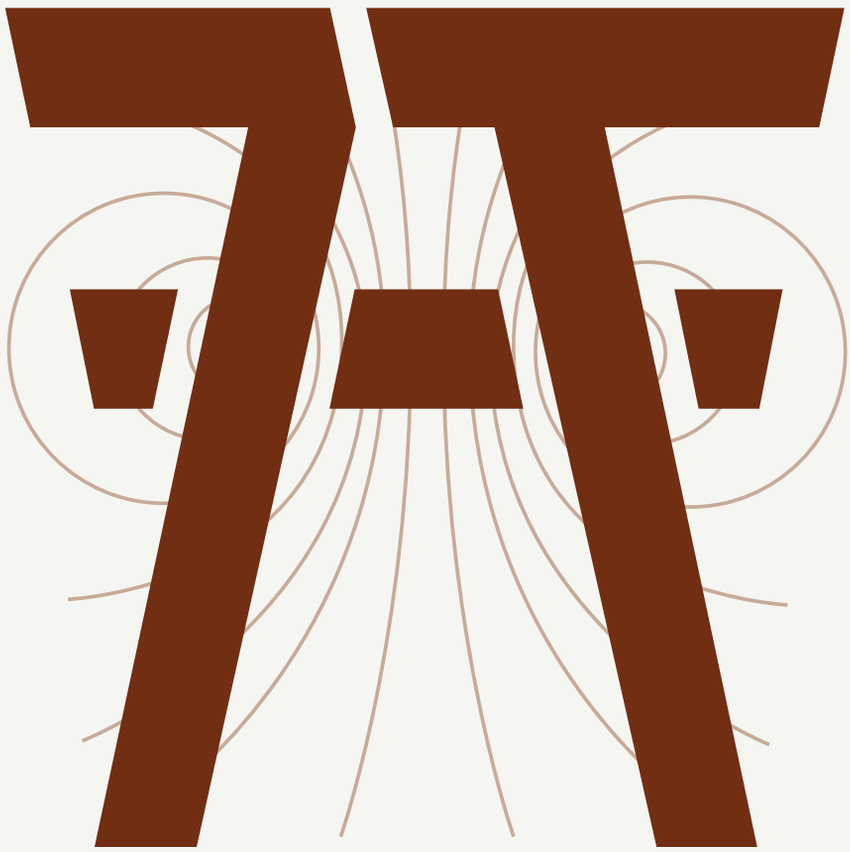

UNIVERSITÄT DUISBURG ESSEN
Open-Minded

UMC St Radboud

UNIVERSITÄT DUISBURG ESSEN
INGENIEURWISSENSCHAFTEN

Donders Institute
for Brain, Cognition and Behaviour

Universitätsklinikum Essen

Radboud Universiteit